Pushing up the easy-axis magnetic anisotropy and relaxation times in trigonal prismatic Co^{II} mononuclear SMMs by molecular structure design

Aritz Landart,[a†] María Mar Quesada-Moreno,[a†] María A. Palacios,[*a] Ismael F. Díaz Ortega,[b,c] Hiroyuki Nojiri,[b] Mykhaylo Ozerov,[d] J. Krzystek,[d] Enrique Colacio[*a]

[a]*Departamento de Química Inorgánica, Facultad de Ciencias, Universidad de Granada, 18071 Granada, Spain. E-mail: ecolacio@ugr.es, mpalacios@ugr.es*

[b]*Institute for Materials Research, Tohoku University, Katahira, Sendai, 980-8577, Japan.*

[c]*Departamento de Química y Física-CIESOL, Universidad de Almería, Ctra. Sacramento s/n, 04120, Almería.*

[d]*National High Magnetic Field Laboratory, Florida State University, Tallahassee, Florida 32310, USA.*

† These authors contributed equally to this work.

EXPERIMENTAL SECTION

Synthetic procedures

All reactions were conducted in aerobic conditions and the analytical reagents were purchased from commercial sources and used without further purification. The precursor tris(methylhydrazido)phosphorylsulfide, $(S)P[N(Me)NH_2]_3$ and the ligand $(S)P[N(Me)N=C(H)(C_3H_2N(Me)N)]_3$ were prepared according to a previously described procedure.[1]

Synthesis of the ligand $(S)P[N(Me)N=C(H)(C_3H_2N(Me)N)]_3$

To a methanolic solution (20 mL) of tris(methylhydrazido)phosphorylsulfide (0.8 g, 4 mmol) was added 1-methylimidazole-2-carbaldehyde (1.3 g, 12 mmol) in 20 mL of methanol and a few drops of acetic acid. The resulting solution was refluxed for 8 hours and after was stirred at room temperature for 16 hours more. Then, the solution was evaporated to dryness and the yellow oil was extracted in dichloromethane. Finally, the organic layer was dried with sodium sulphate and evaporated to dryness. The resulting oil was allowed to let stand at room temperature 48 hours, whereupon the ligand precipitates as a yellow powder. Yield: 68%. Anal. Calc. for $C_{18}H_{27}N_{12}PS$: C, 45.56; H, 5.74; N, 35.42. Found: C, 45.53; H, 5.76; N, 35.27. IR (cm^{-1}): 3100-2800, ν(C-H); 1600-1400, ν(C=C and C=N); 900, ν(P=S) and 800-700, δ(CH).

Synthesis of $[Co(L)](ClO_4)_2$ (1)

To a solution of the ligand (0.05 g, 0.113 mmol) in 10 ml of methanol is added, under stirring, a methanolic solution (10 ml) of $Co(ClO_4)_2 \cdot 6H_2O$ (0.04 g, 0.113 mmol). The product precipitates and is filtered off. The mother solution is left for slow evaporation at room temperature and, after several days, afforded well-formed dark red crystals. Yield: 81%. Anal. Calc. for $C_{18}H_{27}Cl_2CoN_{12}O_8PS$: C, 29.52; H, 3.72; N, 22.95: S, 4.38. Found: C, 29.48; H, 3.68; N, 23.05; S, 4.23. IR (cm–1): 1600-1400, ν(C=C and C=N); 1100, ν(Cl-O); 950, ν(P=S) and 700-800, δ(CH).

Synthesis of $[Co(L)](BF_4)_2$ (2)

A solution of $Co(BF_4)_2 \cdot 6H_2O$ (0.015 g, 0.0423 mmol) in acetonitrile (10 ml) was added to a solution of the ligand (0.02 g, 0.0423 mmol) in 10 ml of acetonitrile and the solution was stirred for 10 minutes. After few days, crystals suitable for X-ray diffraction were obtained by diffusion of isopropanol into the mother liquid. Yield: 80%. Anal. Calc. for $C_{18}H_{27}CoN_{12}F_8PS$: C, 30.58; H, 3.85; N, 23.77: S, 4.54. Found: C, 30.49; H, 4.06; N, 23.73; S, 4.38. IR (cm–1): 1600-1400, ν(C=C and C=N); 1100, 1000 ν(B-F); 950, ν(P=S) and 700-800, δ(CH).

Physical measurements

Elemental analyses were performed on a Fisons-Carlo Erba analyser model EA 1108 and ^{1}H-NMR spectra on a 400 Hz "VARIAN DIRECT DRIVE" spectrometer at the "Centro de Instrumentación Científica" (University of Granada). IR spectra were recorded on a Bruker Tensor 27 spectrophotometer by using ATR detection. The X-ray powder diffraction (XRPD) spectra were registered on a (2θ) Bruker D2-PHASE using CuKα (λ = 1.5418 Å) radiation and LINXEYE detector, from 5 to 50° (2θ) at a scanning rate of 0.5° 2θ/min.

Magnetic Properties

The *dc* magnetic measurements were performed on polycrystalline samples of **1-2,** in the temperature range 2 - 300 K under a magnetic field of 0.1 T using a Quantum Design SQUID MPMS XL-5. Alternating-current (ac) susceptibility measurements under different applied static fields (0-0.3 T) were carried out using a Quantum Design SQUID MPMS XL-5 magnetometer on polycrystalline samples in the temperature range 2-25 K. The measurements were performed under an oscillating field of 5 Oe and *ac* frequencies in the 1-1482 Hz range. The magnetic susceptibility values were corrected for the diamagnetism of the molecular constituents and sample holder.

FIRMS

Far-infrared magnetic spectroscopy (FIRMS, also known as frequency-domain THz EPR spectroscopy[2]) experiments were performed at the National High Magnetic Field Laboratory

using a Bruker Vertex 80v FT-IR spectrometer coupled with a 17 T vertical-bore superconducting magnet in a Voigt configuration (light propagation perpendicular to the external magnetic field). The experimental setup employs broad band terahertz radiation emitted by a mercury arc lamp. The radiation transmitted through the sample was detected by a composite silicon bolometer (Infrared Laboratories) mounted at the end of the quasioptical transmission line. Both sample and bolometer were cooled by a low-pressure helium gas to the temperature of 5 K. The intensity spectra of the microcrystalline powder sample (~2 mg) bonded by n-eicosane were measured in the spectral region between 14 and 730 cm^{-1} (0.42−22 THz) with an instrumental resolution of 0.3 cm^{-1} (9 GHz). To discern the magnetic absorptions, the transmission spectrum at each magnetic field was divided by the reference spectrum, which is calculated as the average spectrum for all magnetic fields after removing outlier points at each frequency. Such normalized spectra are only sensitive to tiny transmission changes induced by the magnetic field and exclude a strong nonmagnetic contribution due to vibrational absorptions and an instrumental function. All data analysis routine was implemented by in-house written MATLAB code based on the EPR simulation software package EasySpin.[3]

High-frequency and -field EPR (HFEPR) spectra of compounds **1-2** were recorded at the National High Magnetic Field Laboratory in a 4.5-10 K temperature range on polycrystalline samples (20−25 mg), using a homodyne spectrometer at the EMR facility associated with a 15/17-T superconducting magnet and a frequency range from 52 to 426 GHz. Detection was provided with an InSb hot electron bolometer (QMC Ltd., Cardiff, UK). The magnetic field was modulated at 50 kHz for detection purposes. A Stanford Research Systems SR830 lock-in amplifier converted the modulated signal to *dc* voltage.

Single-Crystal Structure Determinations

Suitable crystals of **1-2** were mounted on a glass fiber and used for data collection. X-ray diffraction data were collected at 100 K using a Bruker D8 Venture diffractometer (MoKα radiation, λ = 0.71073 Å) outfitted with a PHOTON 100 detector. Unit-cell parameters were determined and refined on all observed reflections using APEX2 software.[4] Correction for Lorentz polarization and absorption were applied by SAINT[5] and SADABS[6] programs, respectively.

The structures were solved by direct methods and refined by the full-matrix least-squares method on F2 using OLEX2 program.[7] All non-hydrogen atoms were refined anisotropically. Hydrogen atom positions were calculated and isotropically refined as riding models to their parent atoms. The ClO_4^- and BF_4^- counteranions in structures **1** and **2** are disordered (O3, O4 atoms for **1** and F3, F4 atoms for **2**) and the disorder model was satisfactory. A summary of

selected data collection and refinement parameters can be found in Table S1 and CCDC 2216062-2216063.

Table S1. Crystallographic data for mononuclear complexes **1** and **2**

Compound	**1**	**2**
Formula	$C_{18}H_{27}Cl_2CoN_{12}O_8PS$	$C_{18}H_{27}B_2CoF_8N_{12}PS$
M_r	732.37	707.09
Crystal System	hexagonal	hexagonal
Space Group	$P6_3$	$P6_3$
a (Å)	10.1198(13)	9.9868(4)
b (Å)	10.1198(13)	9.9868(4)
c (Å)	16.131(2)	16.0438(7)
α (°)	90	90
β (°)	90	90
γ (°)	120	120
V (Å^3)	1430.7(4)	1385.77(13)
Z	2	2
Dc (g cm^{-1})	1.700	1.695
μ(MoK$_\alpha$) (mm^{-1})	0.982	0.842
T (K)	100	100
Observed reflections[a]	2376 (2256)	2143 (2096)
R_{int}[a]	0.0667 (0.0300)	0.0286 (0.0210)
Parameters	133	137
GOF	1.041	1.071
R_1[b,a]	0.0381 (0.0316)	0.0276 (0.0265)
wR_2[c,a]	0.0806 (0.0828)	0.0743 (0.0731)
[a] Values in parentheses for reflections with $I > 2\sigma(I)$ [b] $R1 = \sum\|\|Fo\| - \|Fc\|\|/\sum\|Fo\|$ [c] $wR2 = \{\sum [w(F_o^2 - F_c^2)^2] / \sum [w(F_o^2)^2]\}^{½}$		

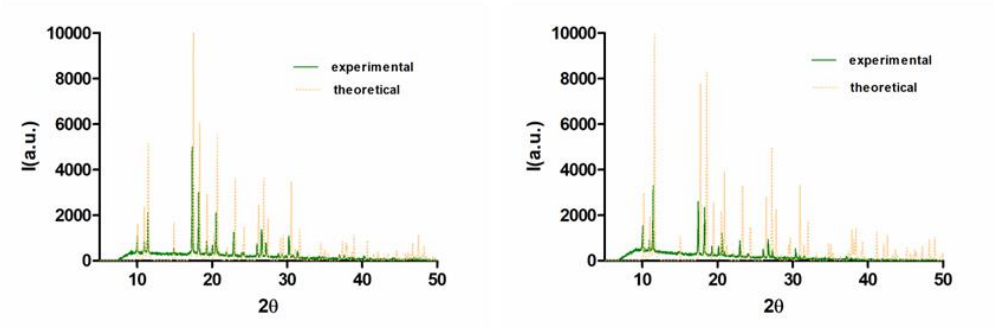

Experimental (green) and theoretical (orange) powder XRD spectra for **1** (left) and **2** (right)

Computational methodology

Calculations were carried out from the crystallographic structures using the cif files. The electronic structure and magnetic properties have been computed using state averaged complete active space self-consistent field calculations (SA-CASSCF (7,5)),[8] followed by the N-electron valence second-order perturbation theory (NEVPT2) method[9] with the def2-TZVPP basis set,[10] including the auxiliary basis sets for correlation and Coulomb fitting for all the atoms. All calculations were done with the ORCA 5.0.2 quantum chemistry program package.[11] Spin Hamiltonian parameters (*D*, *E* and *g*-tensor) were computed using the effective Hamiltonian S=3/2. In this case, spin-orbit effects were included using the quasi-degenerate perturbation theory (QDPT)[12] and scalar relativistic effects were taken into account using the DKH (Douglas-Kroll-Hess) procedure.[13] The employed active space includes seven electrons in five 3d-orbitals of Co^{II} CAS (7,5). We have included all 10 states for the 2S+1= 4 (quartet) states arising from the ^4F and ^4P terms of Co^{II}, and all the 40 states for the respective 2S+1= 2 (duplet) states arising from the ^2P, ^2D (twice), ^2F, ^2G and ^2H terms of the Co^{II} ion. ORCA produces two sets of results CASSCF and NEVPT2. The splitting of d-orbitals due to ligand field has been computed with the *ab initio* ligand field theory (AILFT)[14] module implemented in ORCA program package.

Pulse-field magnetization

Low-temperature magnetization measurements were performed by means of a conventional inductive probe in pulsed-magnetic fields. The temperature was reached as low as 0.4 K using a ^{3}He cryostat.[15] Polycrystalline specimens were mounted in a capillary tube made of polyimide. Samples of approximately 20 mg were not fixed within the sample tube and then they aligned along the magnetic field direction. Subsequently, a magnetic field was applied several times until orientation effect was saturated and the magnetization curves obtained in further shots were found to be identical.

Table S2. Selected bond distances and angles for **1** and **2**, and shape measures for CoN_6 coordination sphere of these complexes.

	Bond Distances (Å)	
	1	**2**
Co-N2	2.225(3)	2.221(2)
Co-N3	2.098(3)	2.096(2)
	Bond Angles (◦)	
	1	**2**
N2-Co-N3	75.71(10)	75.82(8)
N2-Co-N2	81.94(11)	81.80(9)
N3-Co-N3	90.84(11)	90.73(10)
N2-Co-N3	128.17(11)	128.94(8)
N2-Co-N3	138.05(11)	137.38(8)

Complex	**JPPY-6**	**TPR-6**	**OC-6**	**PPY-6**	**HP-6**
1	20.901	0.533	13.593	16.834	35.500
2	20.886	0.486	13.855	16.800	35.444

JPPY-6: Johnson Pentagonal Pyramid J2 (C_{5v}); TPR-6: Trigonal Prism (D_{3h}); OC-6: Octahedron (O_h); PPY-6: Pentagonal Pyramid (C_{5v}); HP-6: Hexagon (D_{6h})

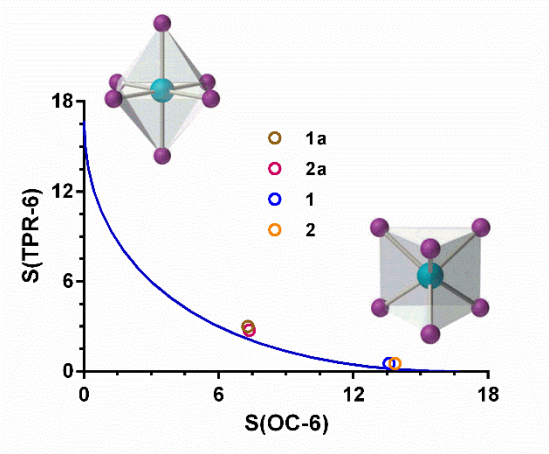

Octahedron-trigonal prism shape map showing the Bailar pathway (blue line) and the experimental data (circles) for **1**, **2**, **1a** and **2a**.

<u>Comparison between the structures of 1, 2, 1a and 2a.</u>

The most significant differences between these compounds and the analogous containing the ligand with the pyridyl moiety, $[Co(L)_2]X_2$ (X = ClO_4^-, **1a** and BF_4^-, **2a**) are: (i) The cationic unit for compounds 1 and **2** has C3 symmetry, whereas in compounds 1a and 2a exhibits C1 symmetry, (ii) The Co-Nimine bond distances are larger and the Co-Nimid shorter in **1** and **2** than in **1a** and **2a**, with a difference between them of 0.12 Å for the former and 0.01 Å for the latter, (iii) The trans Nimine-Co-Nimid bond angles are found in a smaller range (128°-138°) in the former than in the latter compounds (110-150°), (iv) the structures of **1** and **2** are slightly

less truncated and compressed, (iv) the Bailar twist angle of 8.94° and 7.69° for **1** and **2**, respectively, are rather smaller than those found for **1a** and **2a.**

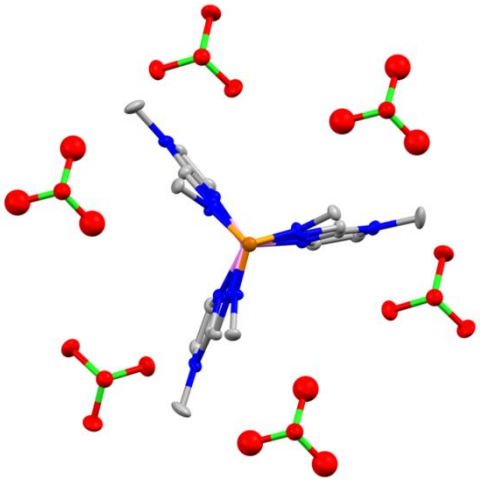

Arrangement of ClO_4^- anions around the $[Co(L1)]^{2+}$ cationic unit of **1**.

Table S3. Spin Free CASSCF/NEVPT2 energies (δE, cm^{-1}). **1'** and **2'** refer to the cationic units $[Co(L1)]^{2+}$.

States	**1**	**2**	**1'**	**2'**
1	0	0	0	0
2	2.6	2.6	2.4	2.3
3	7361.3	7598.7	7456.8	7709.8
4	8169.7	8252.3	8469.0	8566.7
5	8177.7	8259.2	8479.5	8577.0
6	9101.1	9165.8	9329.0	9408.7
7	12086.6	11927.3	12288.1	12137.7

Table S4. Energy levels after the inclusion of spin-orbit effects from CASSCF/NEVPT2 calculations (ΔE, cm^{-1}). **1'** and **2'** refer to the cationic units $[Co(L1)]^{2+}$.

States	**1**	**2**	**1'**	**2'**
1	0	0	0	0
2	299.01	300.09	299.22	300.25
3	631.80	633.64	631.37	633.08
4	993.47	995.76	991.50	993.55
5	7571.47	7781.12	7686.04	7914.46
6	7728.15	7946.92	7843.29	8082.22
7	8471.43	8552.57	8769.56	8866.15
8	8620.71	8700.20	8911.19	9005.02

Table S5. Computed ZFS parameters D, E, |E/D| and *g* values for the ground state. **1'** and **2'** refer to the cationic units $[Co(L1)]^{2+}$. δE_1 and ΔE_1 are the calculated first excitation energies before and after considering spin-orbit effects, respectively.

Compound	**Method**	***D* (cm^{-1})**	***E/D***	***E* (cm^{-1})**	**δE_1 (cm^{-1})**	**ΔE_1 (cm^{-1})**	**g_x, g_y, g_z[a] g'_x, g'_y, g'_z[b]**
1	CASSCF/ NEVPT2	-149.500	0.004272	-0.639	2.6	299.0	1.31, 1.31, 3.51 0.03, 0.03, 9.77
2	CASSCF/ NEVPT2	-150.040	0.003352	-0.503	2.6	300.1	1.30, 1.30, 3.51 0.02, 0.02, 9.77
1'	CASSCF/ NEVPT2	-149.608	0.004321	-0.646	2.4	299.2	1.30, 1.30, 3.50 0.03, 0.03, 9.76
2'	CASSCF/ NEVPT2	-150.125	0.003403	-0.511	2.3	300.3	1.30, 1.30, 3.51 0.02, 0.02, 9.77

[a] *g*-Tensor for the true spin S = 3/2. [b] Effective *g'*-tensors assuming a pseudospin S = 1/2.

Table S6. The ligand field one electron eigenfunctions for **1** and **2** from CASSCF/NEVPT2 calculations.

Compound 1

Orbital	**Energy (eV)**	**Energy (cm^{-1})**	d_{z^2}	d_{xz}	d_{yz}	$d_{x^2-y^2}$	d_{xy}
1	0.000	0.0	0.999858	-0.002332	0.000200	-0.011542	0.012077
2	0.207	1665.9	-0.014427	-0.148513	0.106082	-0.948879	0.257119
3	0.207	1669.2	-0.008710	-0.105620	-0.147317	0.257377	0.949117
4	0.897	7230.8	0.000725	-0.940166	0.287722	0.151896	-0.101149
5	0.901	7266.2	0.000171	-0.287873	-0.940351	-0.100892	-0.150631

Compound 2

Orbital	**Energy (eV)**	**Energy (cm^{-1})**	d_{z^2}	d_{xz}	d_{yz}	$d_{x^2-y^2}$	d_{xy}
1	0.000	0.0	0.999999	-0.000132	0.000148	-0.001069	-0.000493
2	0.199	1603.4	-0.001080	-0.004326	0.165519	-0.640879	-0.749571
3	0.199	1605.9	0.000507	0.165748	0.004189	0.749527	-0.640874
4	0.900	7261.8	0.000038	0.208673	0.963871	0.074766	0.147712
5	0.901	7267.7	-0.000037	-0.963828	0.208660	0.147959	-0.074866

Table S7. Contributions to *D*-tensor of **1** and **2** from CASSCF/NEVPT2 calculations.

	1		**2**	
	D	*E*	*D*	*E*
$^4\Phi_1$	-168.868	-0.000	-169.268	0.002
$^4\Phi_2$	2.762	-2.761	2.588	-2.587
$^4\Phi_3$	4.369	2.725	4.627	-1.064
$^4\Phi_4$	4.574	-2.711	4.433	1.089
$^4\Phi_5$	2.505	2.504	2.415	2.414

Table S8. Magnetic anisotropy, dc and relaxation parameters for complexes **1**-**2**.

Compound	D_{mag} (cm^{-1}) g_{par} g_{perp} |E|	$\|D_{FIRMS}\|$ (cm^{-1})	D_{cal} (cm^{-1})	U_{eff}(K)[a]	τ_0 (s)	C ($s^{-1}K^{-n}$)	n	QTM (s)	H (Oe)
1	95.2 2.246(2) 3.043 (1) 0.22(5)	114.5	-112.6	55 (2)	$3.2(1)\cdot10^{-6}$	0.014 (5)	4.8 (1)	$1.3\ (2)\cdot10^{-3}$	0
				79(1)	$1.1(1)\cdot10^{-6}$	0.0015(4)	5.52 (9)	-	1200
2	98.9 2.226(3) 3.012 (2) 0.61(6)	114.5	-113.6	59 (2)	$3.2(2)\cdot10^{-6}$	0.01 (3)	4.9 (1)	$1.4\ (2)\cdot10^{-3}$	0
				92 (1)	$5.6(5)\ x10^{-7}$	0.00028(5)	6.05(4)	-	1200

[a] Virtual values extracted from the Arrhenius plot using high temperature relaxation times

Table S9. Anisotropic magnetic parameters for trigonal prismatic Co^{II} MSMMs

Compuesto	**D_{exp}[a] (cm^{-1})**	**D_{cal} (cm^{-1})**	**Zero field**	**Reference**
$[Co(tppm)][ClO_4]_2\cdot2CH_3CN\cdot H_2O$	-82	--	Yes	[16] *Eur. J. Inorg. Chem.* **2016**, *2016* (29), 4835–4841
$[Co(P(S)\{[N(CH_3)NCHC_3N_2H_3]_3)\}][(NO_3)_2]$	-72	-141	Yes	[17] *J. Am. Chem. Soc.* **2013**, *135* (18), 7010–7018
α-Co	-111	-103	Yes	[18] *J. Phys. Chem. Lett.* **2016**, *7* (20), 4111–4116
β-Co	-74	-105	Yes	[18] *J. Phys. Chem. Lett.* **2016**, *7* (20), 4111–4116
$(NHEt)_3[Co^{II}Co^{III}_3(L1)_6]$ (2R)	-25	-34	Yes	[19] *Inorg. Chem.* **2015**, *54* (11), 5475–5486
$(NHEt)_3[Co^{II}Co^{III}_3(L2)_6]$ (4R)	-22	29	Yes	[19] *Inorg. Chem.* **2015**, *54* (11), 5475–5486
$(NHEt)_3[Co^{II}Co^{III}_3(L)_6]$	-115	-107	Yes	[20] *Chem. Sci.* **2013**, *4* (4), 1802–1806
$\{Na[LCo]\}(BPH_4)_3$	-76	-142	Yes	[21] *Chem. Commun.* **2017**, *53* (30), 4211–4214
$[Co^{II}(L)]$	-31	-41	Yes	[22] *Phys. Chem. Chem. Phys.* **2016**, *18* (43), 30135–30143
$[Co^{II}(Pzox)_3(BC_6H_5)]Cl$	-109 -82	-110	Yes	[23] *J. Am. Chem. Soc.* **2015**, *137* (31), 9792–9795
$[Co(L)][CoCl_4]\cdot CH_3CN$	-61 D_{FIRMS}= -77	-92	No	[1] *Inorg. Chem. Front.*, **2022**, 9, 2810
$[Co(L)][ZnCl_4]\cdot CH_3OH$	-87 D_{FIRMS}= -94	-91	No	[1] *Inorg. Chem. Front.*, **2022**, 9, 2810
$[Co(L)](ClO_4)_2\cdot2CH_3OH$	-117 D_{FIRMS} = -98	-108	Yes[b]	[1] *Inorg. Chem. Front.*, **2022**, 9, 2810
$[Co(L)](BF_4)_2$	-128 D_{FIRMS} = -101	-110	Yes[b]	[1]*Inorg. Chem. Front.*, **2022**, 9, 2810
[LCoYCoL](NO$_3$)	-39	-	No	[24]*Inorg. Chem.* **2019**, *58*, 1, 756–768
$[Co(tppm)][ClO_4]_2\cdot2CH_3CN\cdot H_2O$	-81	-124	Yes	[25] *Inorg. Chem.*, **2018**, 57, 14047-14051
$[Co(L)](ClO_4)$	$D_{THz-EPR}$= -103	-83	Yes	[26] *ChemPhysChem*, **2019**, 20, 1001-1005

$[Co(AcPyOx)_3BC_6H_5]ClO_4$	-86	-78	Yes	[27] *Inorg. Chem.* **2017**, 56, 6943−6951
$[Co(PzOx)_3(BC_6H_5)DMF]_2(B_{10}Cl_{10})$	-85	-	Yes	[28] *Inorg. Chem.* **2020**, 59, 5845–5853
$[CoTp^{py}]PF_6$	-156[c]	-151[c]	Yes	[29] *Chem. Commun*. **2020**, 56, 8492-8495
$[Co(neo)(ac)_2]$	Δ_{ax} = -3317[d]	Δ_{ax} = -4322[d]	No	[30] *Materials*, **2022**, 15, 1064
$LCoCl_2$	-67	-	-	[31] *Inorg. Chem.* **2020**, 59, 15, 10746–10755
$[Co(hpy)][BPh_4]_2 \cdot 3CH_2Cl_2$	-108	-114	Yes	[32] *Inorg. Chem.* **2020**, 59, 12, 8505–8513

[a] Obtained using the dc magnetic measurements, apart from D_{FIRMS}, which were extracted by FIRMS or THz-EPR.

[b] For the magnetic diluted compounds containing a Co/Zn = 1/6 ratio.

[c] Obtained using the Hamiltonian: $\hat{H} = \alpha\lambda\hat{L}\hat{S} + \alpha^2 B_2^0\left(3\hat{L}_z{}^2 - \hat{L}^2\right) + \beta H(-\alpha\hat{L} + g_e\hat{S})$

[d] Obtained using the Hamiltonian: $\hat{H} = -\alpha\cdot\lambda\left(\vec{S}\cdot\vec{L}\right) + \Delta_{ax}\left(\hat{L}_z{}^2 - \frac{\hat{L}^2}{3}\right) + \Delta_{rh}\left(\hat{L}_x{}^2 - \hat{L}_y{}^2\right) + \mu_B\vec{B}\left(g_e\vec{S} - \alpha\vec{L}\right)$

Table S10. Composition of the eigenvectors for **1** obtained from CASSCF/NEVPT2 calculations. The coefficients give the composition of the wavefunction.

STATE	E (cm^{-1})	Weight	Root	Spin	Ms
1	0.00	0.493	0	3/2	3/2
		0.491	1	3/2	3/2
2	0.00	0.493	0	3/2	-3/2
		0.491	1	3/2	-3/2
3	299.01	0.500	0	3/2	1/2
		0.492	1	3/2	1/2
4	299.01	0.500	0	3/2	-1/2
		0.492	1	3/2	-1/2
5	631.80	0.476	0	3/2	1/2
		0.483	1	3/2	1/2
		0.016	0	3/2	-1/2
		0.017	1	3/2	-1/2
6	631.80	0.016	0	3/2	1/2
		0.017	1	3/2	1/2
		0.476	0	3/2	-1/2
		0.483	1	3/2	-1/2
7	993.47	0.496	0	3/2	3/2
		0.499	1	3/2	3/2

8	993.47	0.496	0	3/2	-3/2
		0.499	1	3/2	-3/2
9	7571.47	0.847	2	3/2	3/2
		0.097	5	3/2	3/2
		0.023	3	3/2	1/2
		0.023	4	3/2	1/2
10	7571.47	0.023	3	3/2	-1/2
		0.023	4	3/2	-1/2
		0.847	2	3/2	-3/2
		0.097	5	3/2	-3/2
11	7728.15	0.022	3	3/2	3/2
		0.021	4	3/2	3/2
		0.850	2	3/2	1/2
		0.011	5	3/2	1/2
		0.010	2	3/2	-1/2
		0.038	3	3/2	-1/2
		0.037	4	3/2	-1/2
12	7728.15	0.010	2	3/2	1/2
		0.038	3	3/2	1/2
		0.037	4	3/2	1/2
		0.850	2	3/2	-1/2
		0.011	5	3/2	-1/2
		0.022	3	3/2	-3/2
		0.021	4	3/2	-3/2
13	8471.43	0.504	3	3/2	3/2
		0.488	4	3/2	3/2
14	8471.43	0.504	3	3/2	-3/2
		0.488	4	3/2	-3/2
15	8620.71	0.025	2	3/2	3/2
		0.019	5	3/2	3/2
		0.012	6	3/2	3/2
		0.395	3	3/2	1/2
		0.364	4	3/2	1/2
		0.085	3	3/2	-1/2
		0.080	4	3/2	-1/2
16	8620.71	0.085	3	3/2	1/2
		0.080	4	3/2	1/2
		0.395	3	3/2	-1/2

	0.364	4	3/2	-1/2
	0.025	2	3/2	-3/2
	0.019	5	3/2	-3/2
	0.012	6	3/2	-3/2

Table S11. Composition of the eigenvectors for **2** obtained from CASSCF/NEVPT2 calculations. The coefficients give the composition of the wavefunction.

STATE	E (cm^{-1})	Weight	Root	Spin	Ms
1	0.00	0.483	0	3/2	3/2
		0.481	1	3/2	3/2
		0.017	0	3/2	-3/2
		0.017	1	3/2	-3/2
2	0.00	0.017	0	3/2	3/2
		0.017	1	3/2	3/2
		0.483	0	3/2	-3/2
		0.481	1	3/2	-3/2
3	300.09	0.500	0	3/2	-1/2
		0.492	1	3/2	-1/2
4	300.09	0.500	0	3/2	1/2
		0.492	1	3/2	1/2
5	633.64	0.014	0	3/2	1/2
		0.014	1	3/2	1/2
		0.478	0	3/2	-1/2
		0.486	1	3/2	-1/2
6	633.64	0.478	0	3/2	1/2
		0.486	1	3/2	1/2
		0.014	0	3/2	-1/2
		0.014	1	3/2	-1/2
7	995.76	0.496	0	3/2	-3/2
		0.499	1	3/2	-3/2
8	995.76	0.496	0	3/2	3/2
		0.499	1	3/2	3/2
9	7781.12	0.688	2	3/2	3/2
		0.093	5	3/2	3/2
		0.022	3	3/2	1/2
		0.022	4	3/2	1/2
		0.137	2	3/2	-3/2

		0.019	5	3/2	-3/2
10	7781.12	0.137	2	3/2	3/2
		0.019	5	3/2	3/2
		0.022	3	3/2	-1/2
		0.022	4	3/2	-1/2
		0.688	2	3/2	-3/2
		0.093	5	3/2	-3/2
11	7946.92	0.012	2	3/2	1/2
		0.048	3	3/2	1/2
		0.047	4	3/2	1/2
		0.815	2	3/2	-1/2
		0.013	5	3/2	-1/2
		0.027	3	3/2	-3/2
		0.026	4	3/2	-3/2
12	7946.92	0.027	3	3/2	3/2
		0.026	4	3/2	3/2
		0.815	2	3/2	1/2
		0.013	5	3/2	1/2
		0.012	2	3/2	-1/2
		0.048	3	3/2	-1/2
		0.047	4	3/2	-1/2
13	8552.57	0.503	3	3/2	3/2
		0.489	4	3/2	3/2
14	8552.57	0.503	3	3/2	-3/2
		0.489	4	3/2	-3/2
15	8700.20	0.045	3	3/2	1/2
		0.040	4	3/2	1/2
		0.425	3	3/2	-1/2
		0.402	4	3/2	-1/2
		0.031	2	3/2	-3/2
		0.026	5	3/2	-3/2
		0.016	6	3/2	-3/2
16	8700.20	0.031	2	3/2	3/2
		0.026	5	3/2	3/2
		0.016	6	3/2	3/2
		0.425	3	3/2	1/2
		0.402	4	3/2	1/2
		0.045	3	3/2	-1/2
		0.040	4	3/2	-1/2

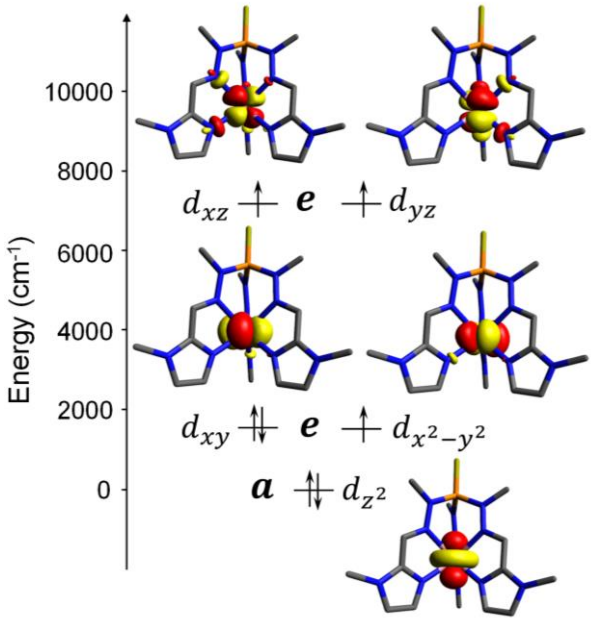

Figure S1. NEVPT2-AILFT computed d-orbital energy diagram of the Co^{II} in complex **1**. Hydrogen atoms and counteranions are omitted for clarity.

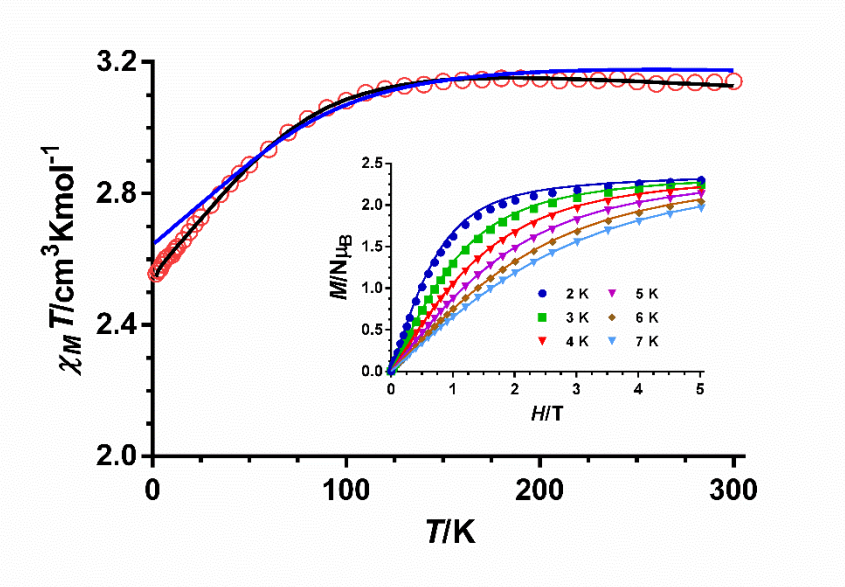

Figure S2. Temperature dependence of $\chi_M T$ and field dependence of the magnetization (inset) for compound **1**. The solid black line (and colourful lines in the inset) represent the best fit to eq. 1 and the blue line the *ab initio* calculated values.

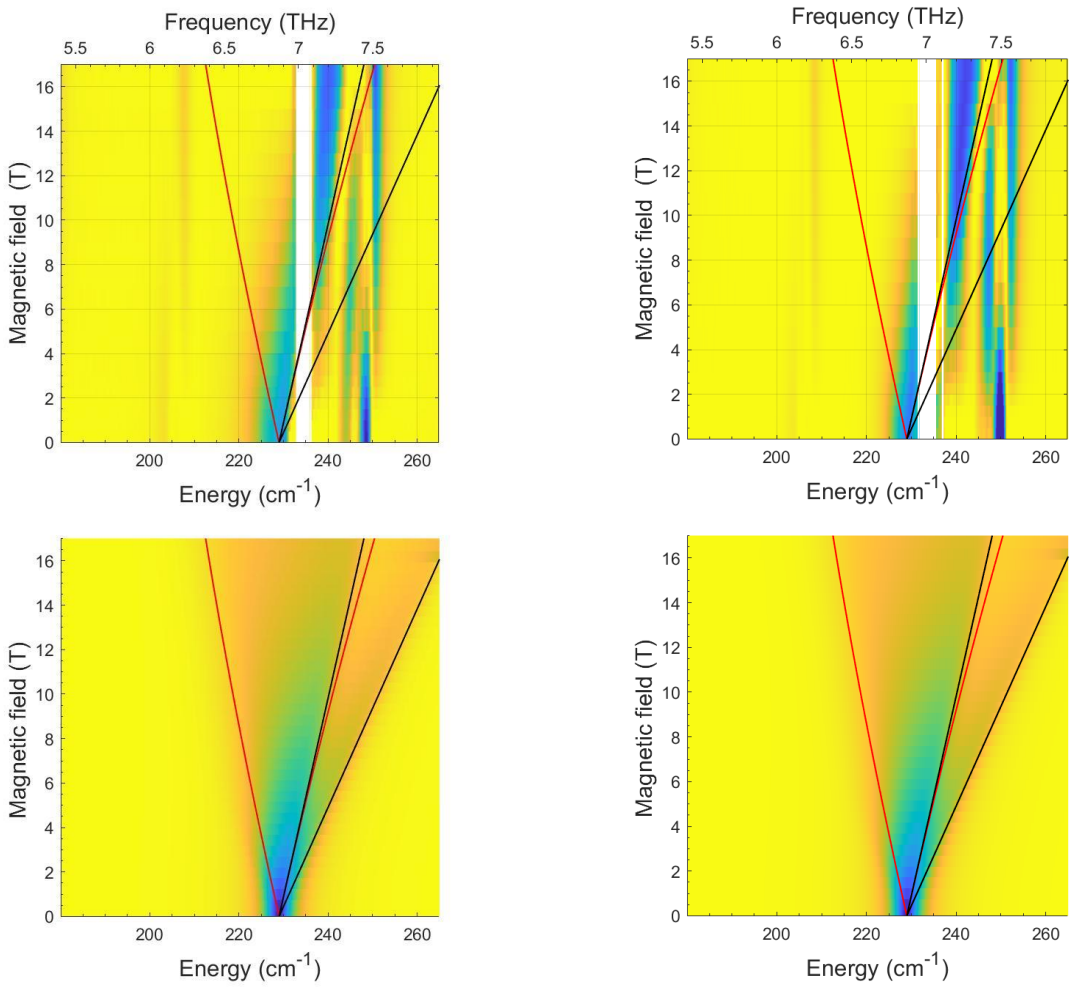

Figure S3. Experimental (top) and simulated (bottom) magnetic field vs. energy heatmaps of FIRMS response for complex **1** (left) **and 2** (right). Blue and yellow regions represent resonance absorptions sensitive to the field. The lines are simulations of turning points for spin Hamiltonian, using S = 3/2, g_{iso} = 2.4 and E = 0.

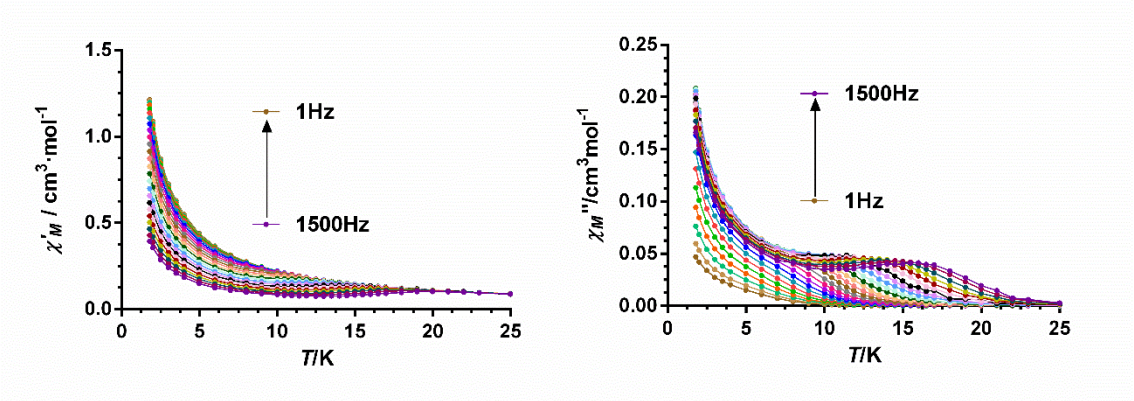

Figure S4. Temperature dependence of the in-phase(χ_M') and out-of-phase (χ_M") ac susceptibilities under zero-field and in the 1Hz-1500 Hz range for compound **2**. Solid lines are only a guide for the eyes.

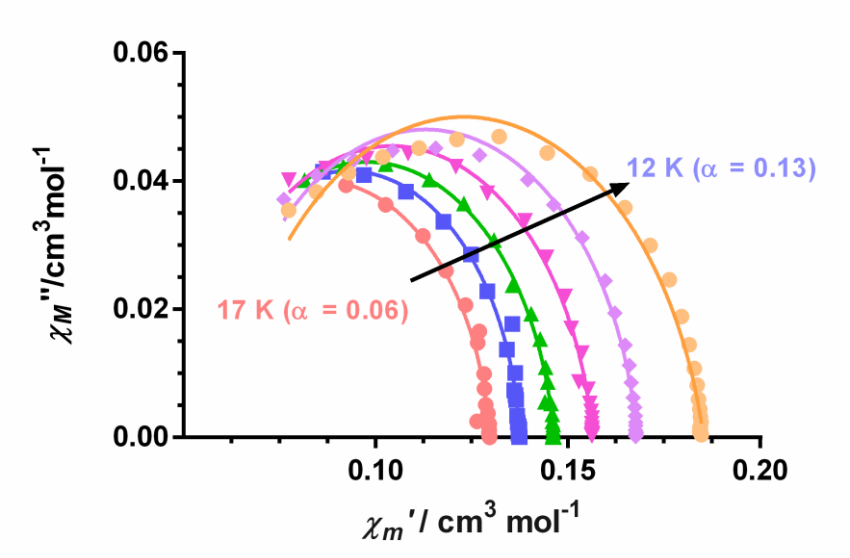

Figure S5. Cole-Cole diagrams for **2** under zero field at the indicated temperatures.

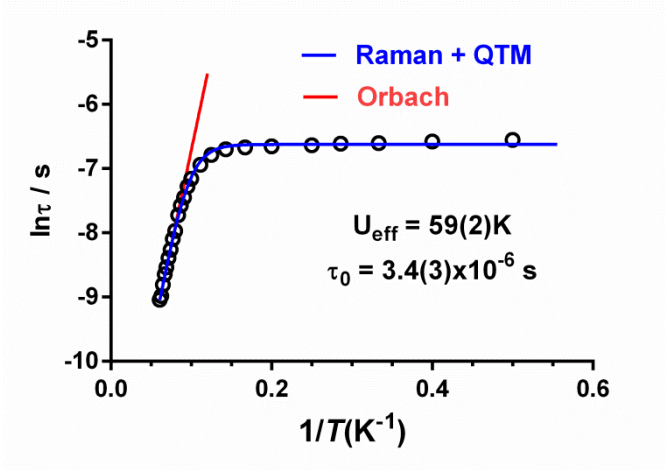

Figure S6. lnt vs 1/T plot for **2** under zero field. The solid red and blue lines correspond to the indicated processes.

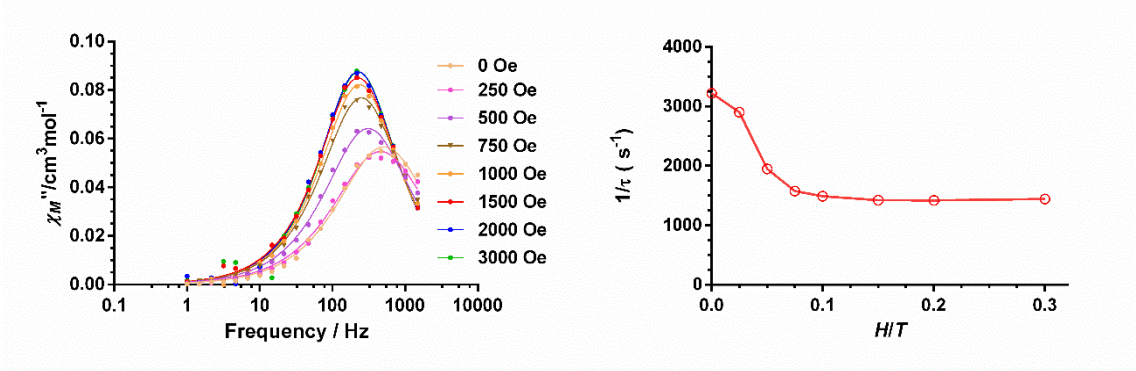

Figure S7. Frequency dependence of the out-of-phase (χ_M") ac susceptibility (left) and field dependence of 1/tau (right) for **2** at 13 K. The solid lines represent the best fit to the generalized Debye model.

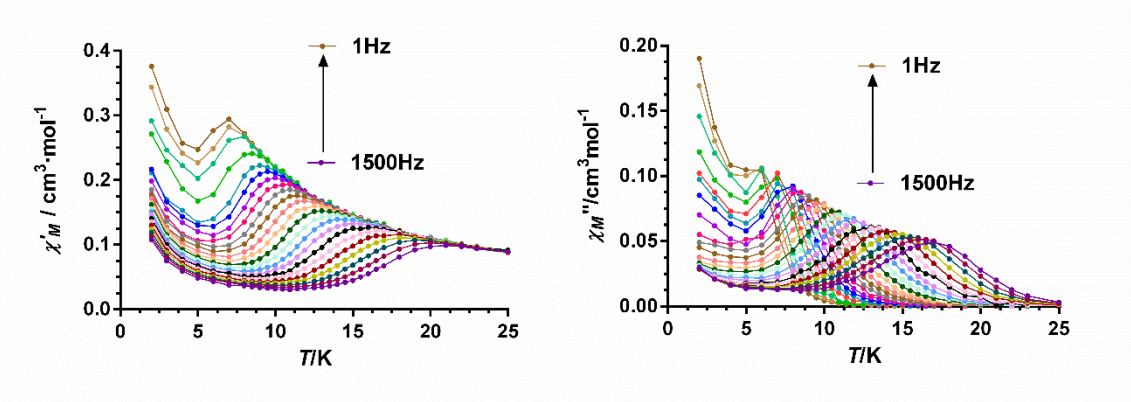

Figure S8. Temperature dependence of the in-phase(χ_M') and out-of-phase (χ_M") ac susceptibilities under a dc field of 0.12 T and in the 1Hz-1500 Hz range for compound **2**. The solid lines are a guide for the eyes.

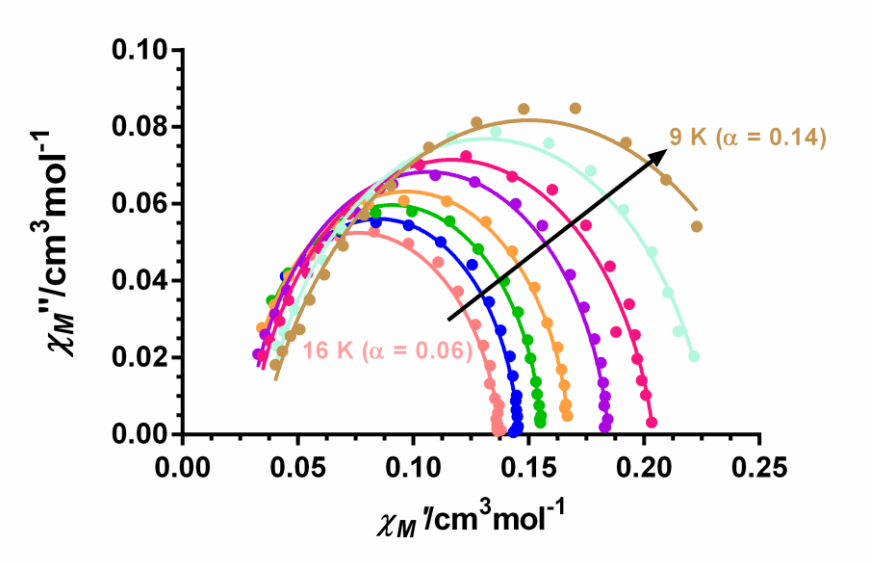

Figure S9. Cole-Cole diagrams for **2** under a dc field of 0.12 T at the indicated temperatures.

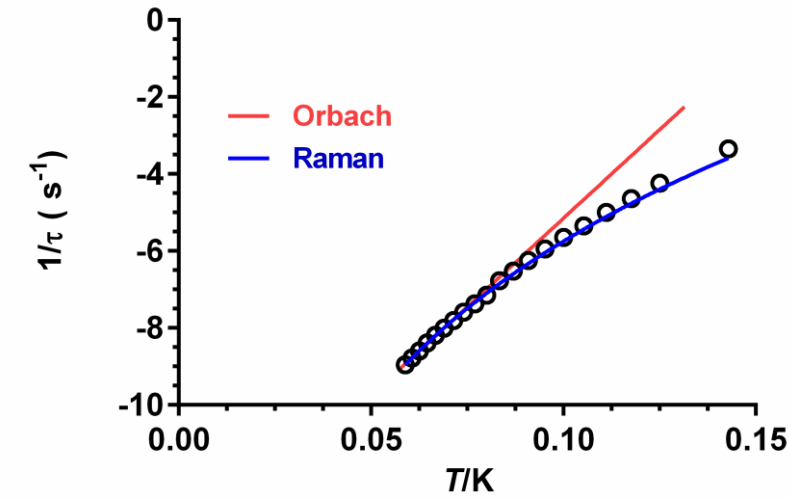

Figure S10. lnt vs 1/T plot for **2** under a dc field of 0.15 T. The solid red and blue lines correspond to the indicated processes.

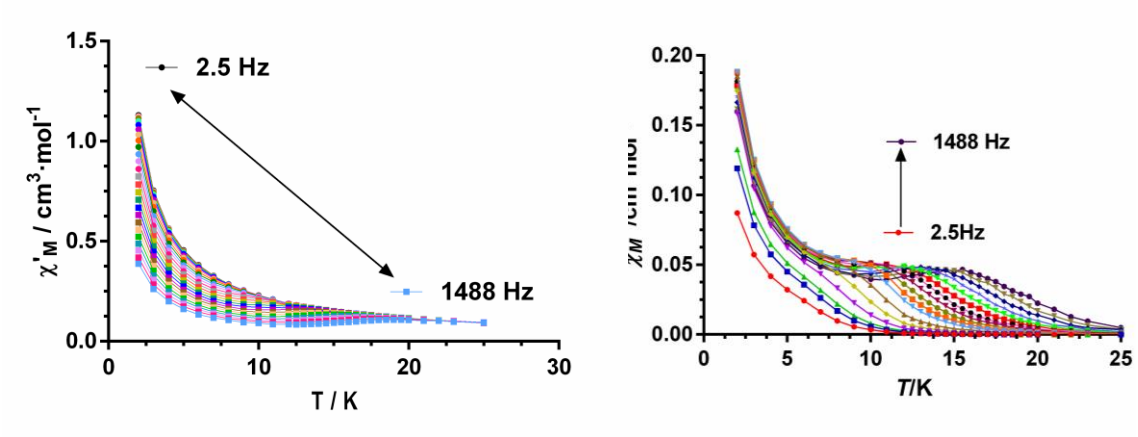

Figure S11. Temperature dependence of the in-phase (χ_M') and out-of-phase (χ_M") ac susceptibilities under zero-field and in the 1Hz-1488 Hz range for compound **1**. The solid lines are a guide for the eyes.

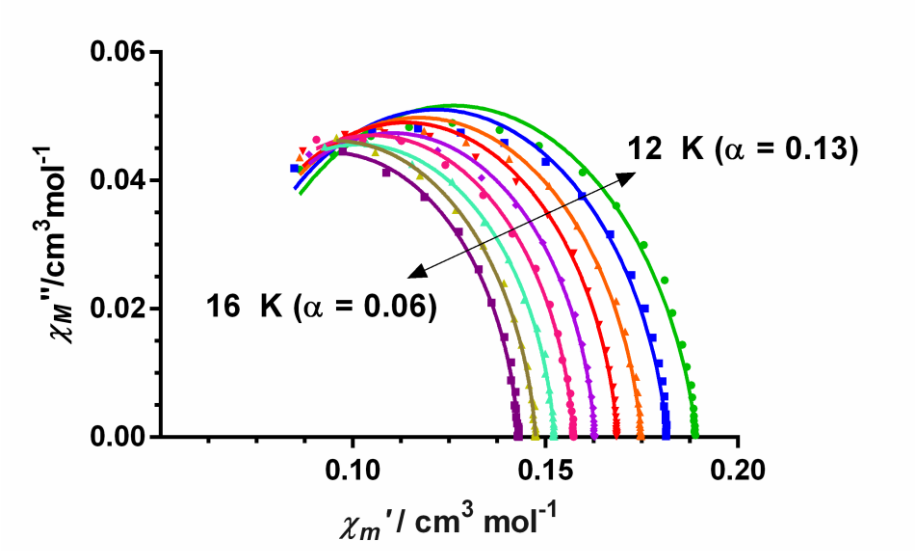

Figure S12. Cole-Cole diagrams for **1** under zero field at the indicated temperatures.

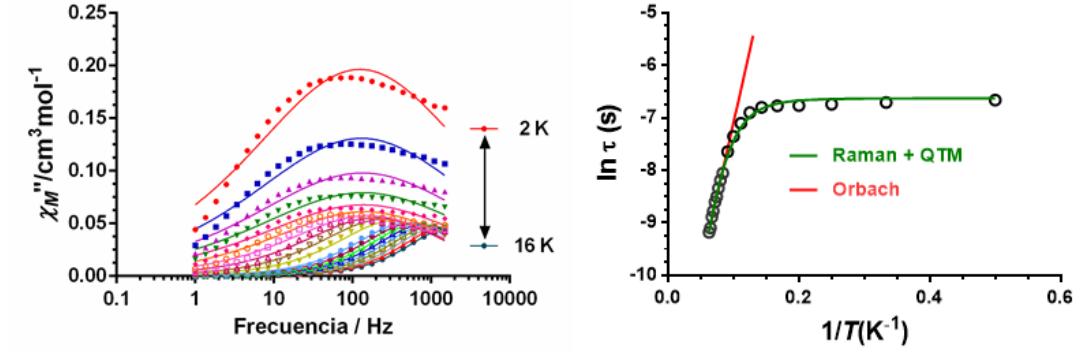

Figure S13. (Left) Frequency dependence of out-of-phase (χ_M") ac susceptibilities at different temperatures for compound **1**. (Right) lnt vs 1/T plot for **1** under zero field. The solid red and green lines correspond to the indicated processes.

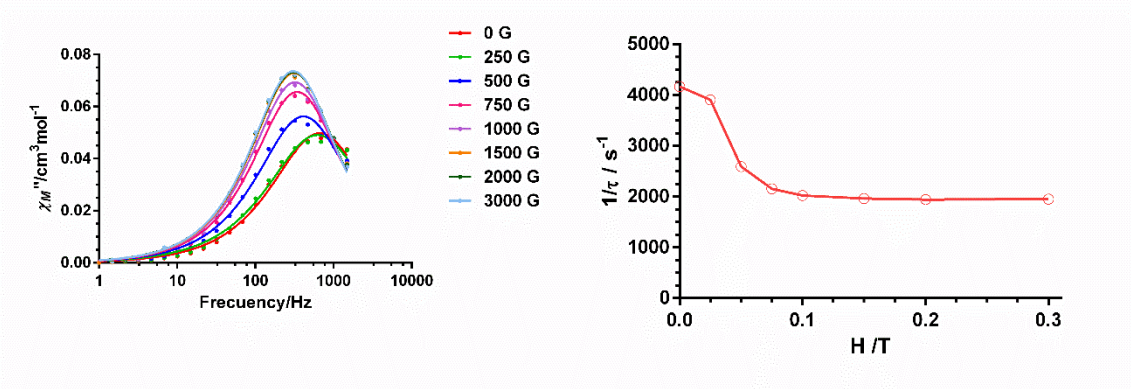

Figure S14. Frequency dependence of the out-of-phase (χ_M") ac susceptibility (left) and field dependence of 1/tau (right) for **1** at 13 K. The solid lines represent the best fit to the generalized Debye model.

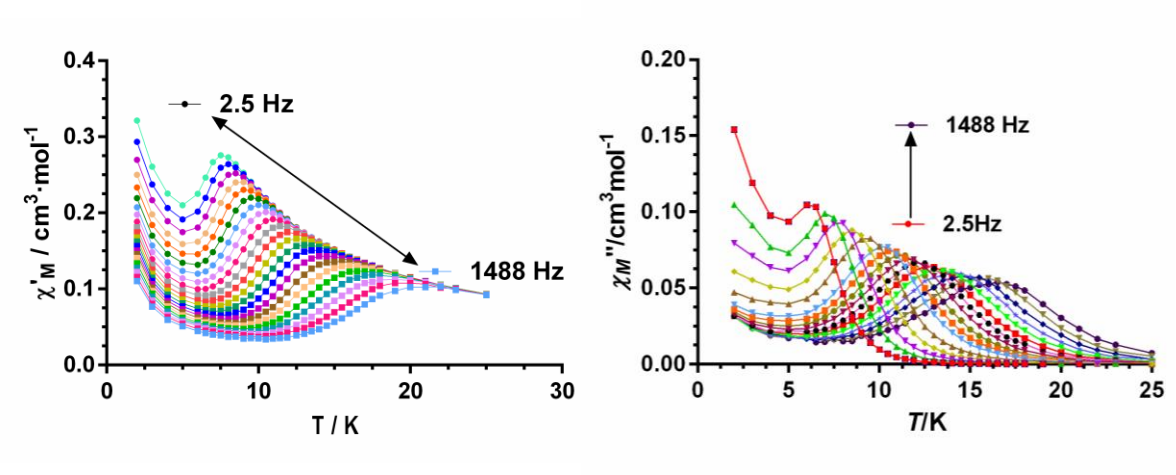

Figure S15. Temperature dependence of the in-phase(χ_M') and out-of-phase (χ_M") ac susceptibilities under a dc field of 0.15 T and in the 1Hz-1500 Hz range for compound **1**. The solid lines are a guide for the eyes.

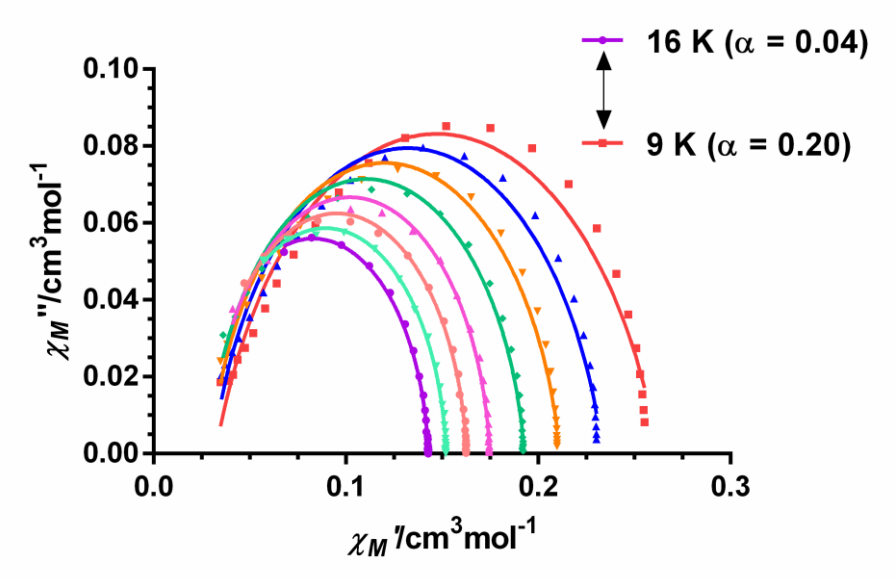

Figure S16. Cole-Cole diagrams for **1** under a dc field of 0.15 T at the .indicated temperatures.

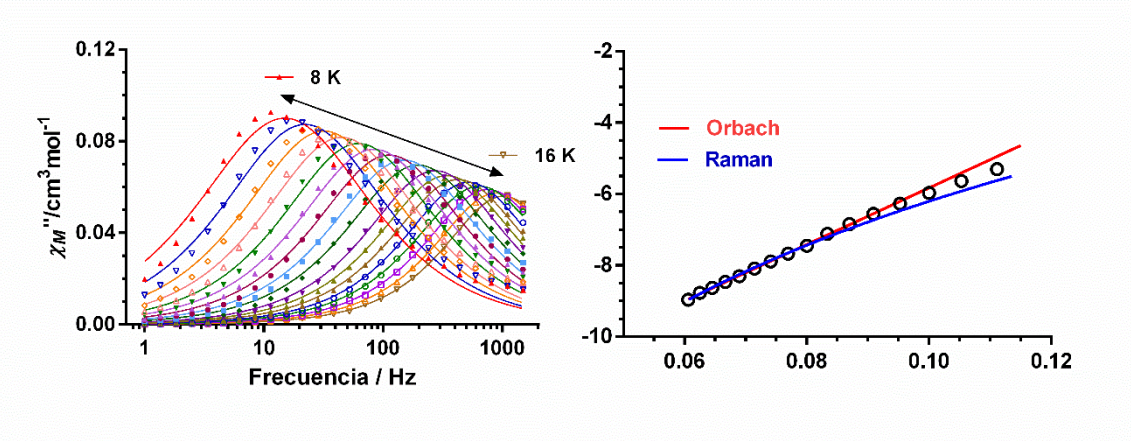

Figure S17. (Left) Frequency dependence of out-of-phase (χ_M") ac susceptibilities at different temperatures for compound **2**. (Right) lnt vs 1/T plot for **1** under a dc field of 0.15 T. The solid red and blue lines correspond to the indicated processes.

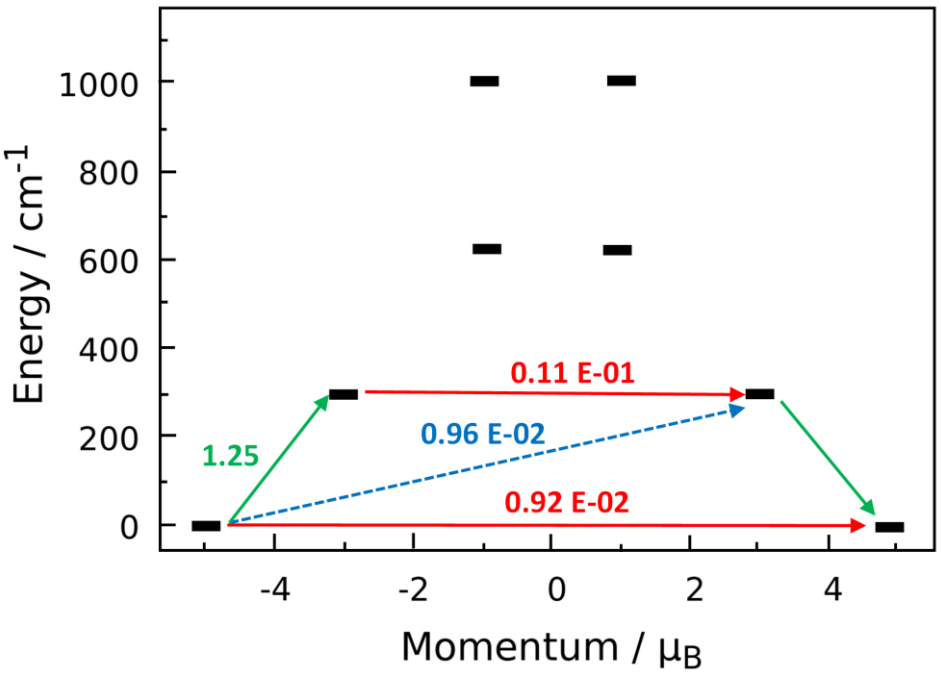

Figure S18. Possible relaxation pathways in **1**. The black lines indicate the KDs as a function of the magnetic moments. Red lines denote QTM in the ground state and TA/QTM through the first excited state. Blue dashed lines represent possible Orbach processes.

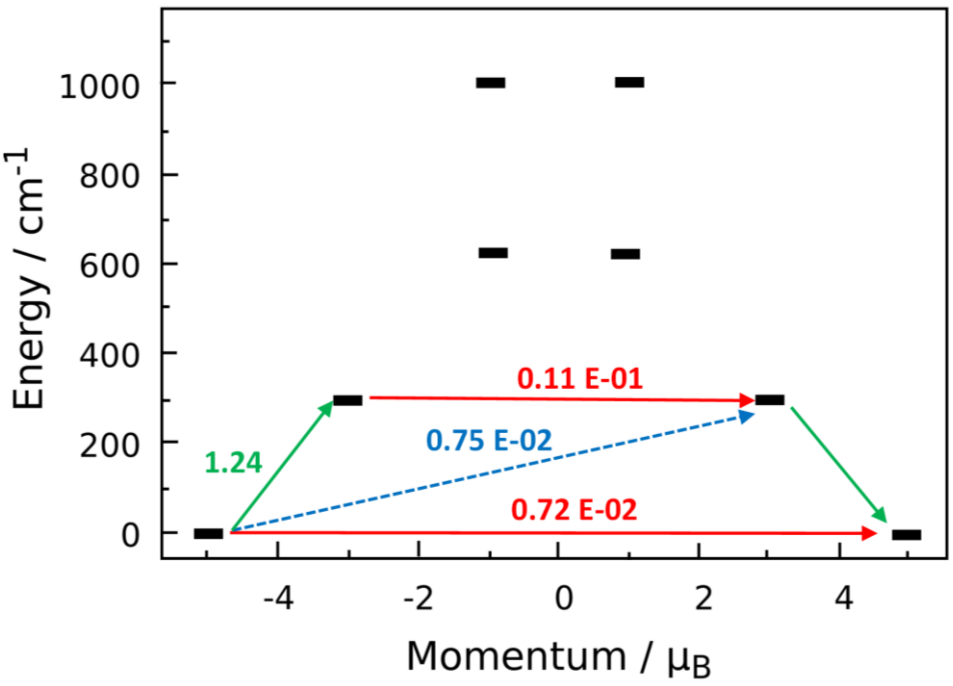

Figure S19. Possible relaxation pathways in **2**. The black lines indicate the KDs as a function of the magnetic moments. Red lines denote QTM in the ground state and TA/QTM through the first excited state. Blue dashed lines represent possible Orbach processes.

Raman mechanism through vibrational modes

To analyse the temperature dependence of the relaxation time, we have considered the contribution of the low energy optical phonons. For it, in the presence of an optimal field of 0.15 T to eliminate the QTM, we have used the following equation:

$$\tau^{-1} = D\frac{\exp(\frac{h\omega/2\pi}{k_BT})}{\left[\exp\left(\frac{h\omega/2\pi}{k_BT}\right)-1\right]^2} + Ecoth(\delta/k_BT)$$

where the first term corresponds to the Raman mechanism through the vibrational mode ω and the second term accounts for the direct mechanism between Ms = ±3/2 states. Under the optimal field of 0.15 T these states are not degenerated but they split by an energy of δ/k_BT = 0.6 K. The fits of the τ^{-1} vs T was obtained with hω = 51(1) cm^{-1}, D = 0.92(7) x10^6 s^{-1} and E = 3(1) s^{-1} for **1** and hω = 66(1) cm^{-1}, D = 2.0(2) x10^6 s^{-1} and E = 7(1) s^{-1} for **2**.

In order to analyze the temperature dependence of τ^{-1}at zero field using equation 2, we have fixed hω to the value extracted from the fit of the τ^{-1} vs T data at 0.15 T and replacing the direct

term by the tunneling rate $\tau^{-1}_{QT} = 769 \pm 140\ s^{-1}$ and $\tau^{-1}_{QT} = 714 \pm 120\ s^{-1}$. The τ^{-1} vs T data can be reasonably well reproduced with D = 0.97(3) $x10^6\ s^{-1}$and D = 2.7(2) $x10^6\ s^{-1}$ for **1** and **2**, respectively (see Figure below).

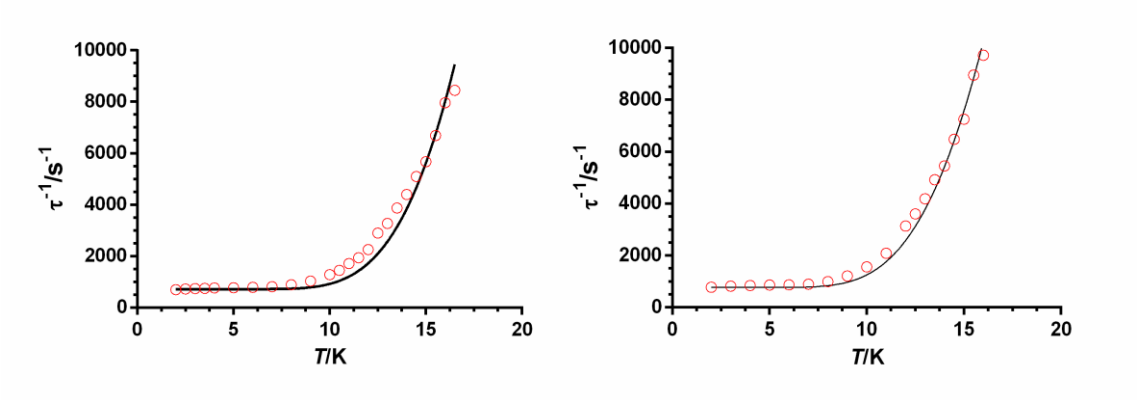

Temperature dependence of relaxation rate for **1** (left) and **2** (right) at zero field. Solid black lines represent the best fit to the Raman mechanism through vibrational modes.

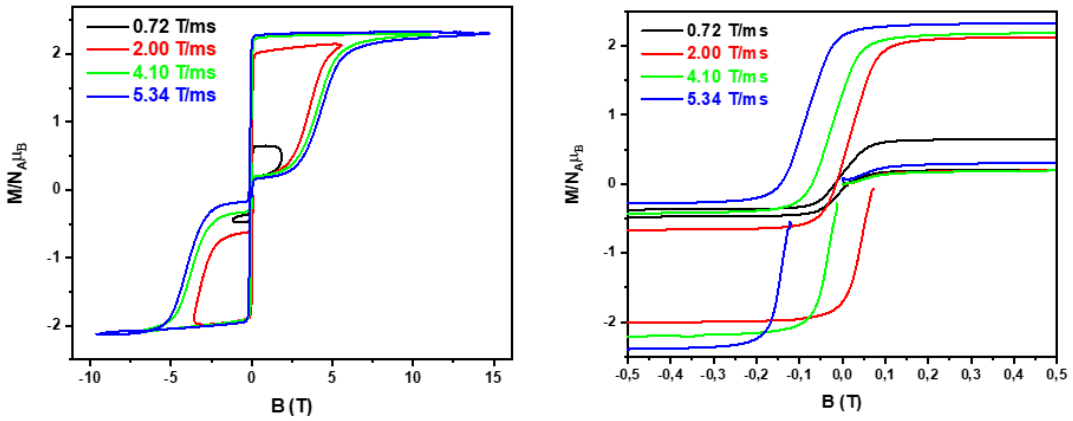

Figure S20. Pulse-field magnetization curves for **1** at 0.4 K at the indicated sweep rates (left). The area close to zero field is zoomed (right). The coercive field (H_c) and remnant magnetization (M_R) at zero field of about 70 G and 1.30 μ_B, respectively, at a sweep rate of 4.10 T/ms.

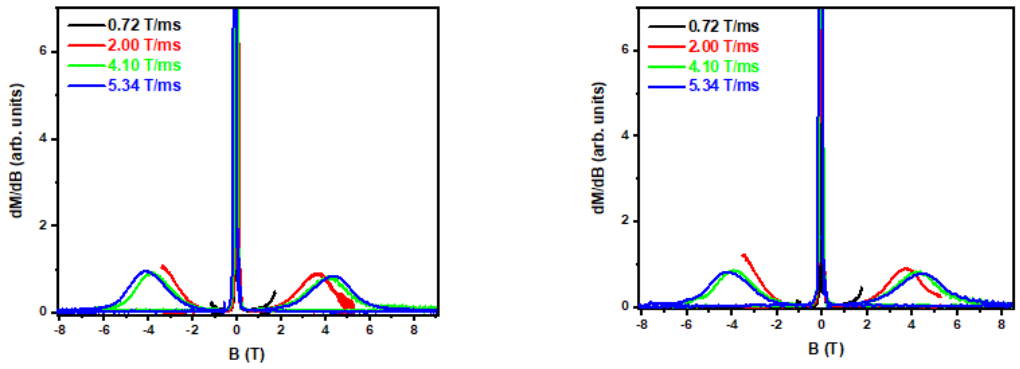

Figure 21. Field dependence of the differential magnetization for **1** (left) and **2** (right).

References

1.- A. Landart-Gereka, M. M. Quesada-Moreno, I. F. Díaz Ortega, H. Nojiri, M. Ozerov, J. Krzystek, M. A. Palacios, E. Colacio, *Inorg. Chem. Front.*, 2022**, 9,** 2810.
2.- J. Nehrkorn, J. Telser, K. Holldack, S. Stoll, A. Schnegg, *J. Phys. Chem. B*, 2015, **119**, 13816.
3.- S. Stoll, A. Schweiger, *J. Magn. Reson.*, 2006, **178**, 42.
4.- APEX2, Bruker AXS, Madison, WI, 2010.
5.- SAINT, Version 8.30a, Bruker AXS, Madison, WI, 2013.
6.- G. M. Sheldrick, SADABS, Version 2004/1, Bruker AXS, Madison, WI, 2008.
7.- O. V. Dolomanov, L. J. Bourhis, R. J. Gildea, J. A. K. Howard, H. Pushman, *J. Appl. Crystallogr.*, 2009, **42**, 339.
8.- P. A. Malmqvist, B. O. Roos, *Chem. Phys. Lett.*, 1989, **155**, 189.
9.- (a) C. Angeli, R. Cimiraglia, J.-P. Malrieu, *Chem. Phys. Lett.*, 2001, **350**, 297; (b) C. Angeli, R. Cimiraglia, S. Evangelisti, T. Leininger, J.-P. Malrieu, *J. Chem. Phys.*, 2001, **114**, 10252; (c) C. Angeli, R. Cimiraglia, J.-P. Malrieu, *J. Chem. Phys.*, 2002, **117**, 9138.
10.- (a) F. Weigend, R. Ahlrichs, *Phys. Chem. Chem. Phys.*, 2005, **7**, 3297; (b) A. Schaefer, H. Horn, R. Ahlrichs, *J. Chem. Phys.*, 1992, **97**, 2571; (c) A. Schaefer, C. Huber, R. Ahlrichs, *J. Chem. Phys.*, 1994, **100**, 5829.
11.- F. Neese, "Software update: The ORCA program system, version 5.0". Wiley Interdisciplinary Reviews: Computational Molecular Science, 2022, **12**, e1606.
12.- (a) D. Ganyushin, F. Neese, *J. Chem. Phys.*, 2013, **138**, 104113; (b) D. Ganyushin, F. Neese, *J. Chem. Phys.*, 2006, **125**, 024103; (c) R. Maurice, R. Bastardis, C. D. Graaf, N. Suaud, T. Mallah, N. Guihéry, *J. Chem. Theory Comput.*, 2009, **5**, 2977; (d) F. Neese, *J. Chem. Phys.*, 2005, **122**, 034107.
13.- T. Nakajima, *Chem. Rev.*, 2012, **112**, 385.
14.- J. Jung, M. Atanasov, F. Neese, *Inorg Chem.*, 2017, **56**, 8802.
15.- H. Nojiri, K.-Y. Choi, N. Kitamura, *J. Magn. Magn. Mater.*, 2007, **310**, 1468.
16.- C. Villa-Pérez, I. Oyarzabal, G. A. Echeverría, G. C. Valencia-Uribe, J. M. Seco, D. B. Soria, *Eur. J. Inorg. Chem.*, *2016* (29), 4835.
17.- S. Gomez-Coca, E. Cremades, N. Aliaga-Alcalde, E. Ruiz, *J. Am. Chem. Soc.* 2013, ***135*** (18), 7010.
18.-A. A. Pavlov, Y. V. Nelyubina, S. V. Kats, L. V. Penkova, N. N. Efimov, A. O. Dmitrienko, A. V. Vologzhanina, A. S. Belov, Y. Z. Voloshin, V. V. Novikov, *J. Phys. Chem. Lett.* 2016, ***7*** (20), 4111.
19.- Y. Y. Zhu, Y. Q. Zhang, T. T. Yin, C. Gao, B. W. Wang, S. Gao, *Inorg. Chem.* 2015, ***54*** (11), 5475.
20.-Y. Y. Zhu, C. Cui, Y. Q. Zhang, J. H. Jia, X. Guo, C. Gao, K. Qian, S. Da Jiang, B. W. Wang, Z. M. Wang, *Chem. Sci.* 2013, ***4*** (4), 1802.
21.- T. J. Ozumerzifon, I. Bhowmick, W. C. Spaller, A. K. Rappé, M. P. Shores, *Chem. Commun.* 2017, ***53*** (30), 4211.

22.- Y. Peng, T. Bodenstein, K. Fink, V. Mereacre, C. E. Anson, A. K. Powell, *Phys. Chem. Chem. Phys.* 2016, ***18*** (43), 30135.
23.- V. V. Novikov, A. A. Pavlov, Y. V. Nelyubina, M. E. Boulon, O. A. Varzatskii, Y. Z. Voloshin, R. E. P. Winpenny, *J. Am. Chem. Soc.* 2015, ***137*** (31), 9792.
24.- J.-P. Costes, G. Novitchi, V. Vieru, L. F. Chibotaru, C. Duhayon, L. Vendier, J.-P. Majoral, W. Wernsdorfer, *Inorg. Chem.* 2019, ***58***, 1, 756.
25.- B. Yao, Y. F. Deng, T. Li, J. Xiong, B. W. Wang, Z. Zheng and Y. Y. Zhang, *Inorg. Chem.*, 2018, **57**, 14047.
26.- A. A. Pavlov, D. Y. Aleshin, S. A. Savkina,, A. S. Belov, N. N. Efimov, J. Nehrkorn, M. Ozerov, Y. Z. Voloshin, Y. V. Nelyubina and V. V. Novikov, *ChemPhysChem*, 2019, **20**, 1001.
27.- A. A. Pavlov, S. A. Savkina, A. S. Belov, Y. V. Nelyubina, N. N. Efimov, Y. Z. Voloshin, V. V. Novikov, *Inorg. Chem*. 2017, **56**, 6943.
28.- A. S. Belov, Y. Z. Voloshin, A. A. Pavlov, Y. V. Nelyubina, S. A. Belova, Y. V. Zubavichus, V. V. Avdeeva, N. N. Efimov, E. A. Malinina, K. Yu. Zhizhin, N. T. Kuznetsov, *Inorg. Chem*. 2020, **59**, 5845.
29.- M. R. Saber, M. K. Singh, K. R. Dunbar, *Chem. Commun*. 2020, **56**, 8492.
30.- Ivan Nemec, O. F. Fellner, B. Indruchová, R. Herchel, *Materials*, 2022, **15**, 1064.
31.- A. A. Pavlov, J. Nehrkorn, S. V. Zubkevich, M. V. Fedin, K. Holldack, A. Schnegg, V. V. *Inorg. Chem.* 2020, **59**, 15, 10746.
32.- B. Yao, M. K. Singh, Y.-F. Deng, Y.-N. Wang, K. R. Dunbar, Y.-Z. Zhang, *Inorg. Chem.* 2020, **59**, 12, 8505.